Dark Current Spectroscopy on Alpha Irradiated Pinned Photodiode CMOS Image Sensors

Jean-Marc Belloir, Vincent Goiffon, Cédric Virmontois, Philippe Paillet, Mélanie Raine, Pierre Magnan, Olivier Gilard

Dark Current Spectroscopy on Alpha Irradiated Pinned Photodiode CMOS Image Sensors

Jean-Marc Belloir, *Student Member, IEEE*, Vincent Goiffon, *Member, IEEE*, Cédric Virmontois, *Member, IEEE*, Philippe Paillet, *Senior Member, IEEE*, Mélanie Raine, *Member, IEEE*, Pierre Magnan, *Member, IEEE*, Olivier Gilard

***Abstract*—Dark Current Spectroscopy is tested for the first time on irradiated CMOS Image sensors (CIS) to detect and identify radiation-induced silicon bulk defects. Two different pinned photodiode CIS are tested: a 5MP Commercial-Off-The-Shelf (COTS) CIS from OmniVision (OV5647) and a 256x256 pixel custom CIS. These CISs are irradiated with alpha particles at various fluences and at two different particle energies in the custom CIS (4 MeV or < 500 keV). Several defect types are detected in both CIS (up to five in the custom CIS). The identity of the defects is investigated by measuring the activation energy of the dark current and the stability of the defects during an isochronal annealing. Two defects are identified in the custom CIS: the divacancy and the vacancy-phosphorus. This work proves that dark current spectroscopy can be used on irradiated CIS to detect and identify radiation-induced silicon bulk defects.**

***Index Terms*—Dark Current Spectroscopy (DCS), Pinned PhotoDiode (PPD), CMOS Image Sensor (CIS), irradiation, radiation-induced defects, traps, dark current, annealing, activation energy.**

I. INTRODUCTION

Radiation environments can severely impact the performance of image sensors such as Coupled Charged Devices (CCD) or Active Pixel Sensors (APS), also called CMOS Image Sensors (CIS). Indeed, they contain particles which can produce displacement damage and lead to the formation of silicon bulk defects in the pixels [1-2]. Some of these defects introduce energy levels in the bandgap of silicon, becoming Shockley-Read-Hall Recombination-Generation (SRH R-G) centers [3] which can generate dark current in the pixel if they are located in the depleted volume of the photodiode. Charged particles also produce ionization, which degrades the oxide silicon interfaces and also leads to a dark current increase from depleted oxide surfaces. However, in Pinned PhotoDiode (PPD) CIS (or in buried channel CCDs), oxide surfaces are passivated and do not touch the depleted volume of the photodiodes, hence the effect of ionization on the dark current increase is expected to be limited compared to displacement damage in this work.

The most critical particles for radiation-induced dark current in space and nuclear environments are those which interact mostly via nuclear scattering in silicon, producing high energy recoils. These recoils produce large damage cascades and lead to high dark current increases in the impacted pixels, which could correspond to the superimposition of dark current contributions from many single defects. An improved knowledge of the radiation-induced single bulk defects in silicon could help modeling the high dark current increases produced by nuclear scattering and improve the dark current increase prediction for space and nuclear environments. The knowledge of the nature of the defects and their atomic components could also give ideas to prevent their formation, for example by adding or removing specific impurities when fabricating the image sensor.

A defect detection method which has not been tested yet on irradiated CIS is the Dark Current Spectroscopy (DCS). This technique was first proposed by R. D. McGrath in 1987 to study dark current in CCDs [4]. It is based on the assumption that a given type of silicon bulk defect has only one possible dark current generation rate and temperature dependence of this rate [3]. Hence, if the generation rate of isolated single defects can be measured, it becomes possible to individually detect and characterize these defects. In order to perform DCS, we need a device which can sample the dark current of very small depleted volumes of silicon which contain single defects. State-of-the-art image sensors such as PPD CIS are great candidates to perform DCS because they contain many independent pixels with ultra-low intrinsic dark current (in the e-/s range), which can sample the dark current generated in very small depleted volumes of silicon. In that case, the most common radiation-induced bulk defects can be detected by peaks in the dark current increase distribution of the image sensor (because all the pixels that contain an identical defect have an identical dark current increase). The DCS is an alternative to (for example) the Deep Level Transient Spectroscopy (DLTS), and can provide a much lower defect concentration detection level because the spectroscopy is performed on a large number of pixels instead of a single test structure. The spatial resolution is also much better because the DLTS requires high capacitances and thus large silicon areas. DCS has first been tested on uncontaminated CCD [4], uncontaminated CIS [5], and on CCD [6, 7] and CIS [8-11] contaminated with metal impurities. Radiation-induced defects have also been studied with DCS in a CCD [12].

The aim of this work is to test DCS on irradiated PPD CIS for the first time. Indeed, PPD CIS has become the main optical imaging technology for a wide variety of consumer and high-end scientific applications; hence it is important to see if DCS can be used for future imagers dedicated to space or nuclear sciences. Moreover, PPD CIS is a technology with

TABLE I: MAIN CHARACTERISTICS OF THE TESTED CIS

CMOS Image CIS	COTS OmniVision OV5647 (CIS A)	Custom (identical CIS B and B')
Technology	TSMC 0.11 µm	0.18 µm
Array size	2592 x 1944 pixels	256 x 256 pixels
Pitch	1.4 µm	4.5 µm
Illumination	Backside	Frontside

very promising performances, especially regarding intrinsic dark current, which could allow high resolution DCS measurements to characterize defects with more precision. Eventually, PPD CIS may contain different dopants and impurities than CCD in the silicon bulk, hence PPD CIS can contain specific radiation-induced defects or their concentrations can be different than in CCD for a same radiation environment.

In order to detect radiation-induced bulk defects by DCS, only one defect must be present in each photodiode. Thus, DCS cannot be tested directly on high-energy proton or neutron irradiated CIS which produce many defects per pixel through high-energy nuclear interactions. Electrons or low-energy light ions such as protons and alphas must be used instead, because they interact mainly via Columbic (Rutherford) scattering which is a low-energy interaction [13, 14]. The ideal particle to perform DCS is the one with the maximum Displacement Damage Dose (DDD) to Total Ionizing Dose (TID) ratio, in order to minimize the ionization induced dark current (which increases the mean and the variance of the dark current, reducing the dark current increase resolution). This ratio, which is equal to the ratio between the Non-Ionizing Energy Loss (NIEL) and the Linear Energy Transfer (LET), is better for alpha particles than for protons (especially at low energies), mainly because the Columbic scattering is much more probable for alphas [15, 16]. Moreover, it was observed that more vacancies (which number is proportional to DDD) survive and lead to stable defects with alphas than with protons [17, 18, 19], possibly because of the higher Columbic scattering probability (leading to a higher vacancy density and thus a higher probability to combine into stable defects such as the divacancy).

Consequently, for this first study of DCS on irradiated CIS, alpha particles were chosen to prove the applicability of the DCS to detect radiation induced defects in CIS, using a particle that will generate single defects in the pixels and allow their detection using DCS. This is the first step toward understanding and modeling the high dark current increases usually observed with particles more typical for space (e.g. protons) or nuclear applications (e.g. neutrons), that may be due to the superimposition of dark current contributions from many defects similar to the single defects detected by DCS in this study.

II. EXPERIMENTAL DETAILS

A. Irradiated CISs

Table I presents the details of the two different CIS irradiated in this study. The first one (CIS A) is a backside-illuminated 5MP COTS CIS (OmniVision OV5647), offering great statistics for DCS measurements thanks to its many pixels. Its pre-irradiation dark current is also very low (30 e^-/s at 60°C, and less than 1 e^-/s at 22°C). The CVF has been determined under illumination using the mean variance method, and the linearity has been verified. The raw images can be extracted, so that some integrated automatic features do not interfere (exposure, white balance and digital gain). However, the analog gain changes between illuminated conditions (in which the CVF was determined) and dark conditions. Indeed, it was observed that an automatic analog gain of 2 seemed to be automatically applied in the dark, instead of one under illumination. Because of this, there is uncertainty in the CVF in the dark and the absolute value of the dark current is not known. Hence, for CIS A, the dark current is represented in Arbitrary Units (A.U.). Moreover, the CIS automatically performs a black level calibration, which applies an offset to the whole image. This offset changes with irradiation because the mean dark signal of the array increases. Hence, the reference of the dark current is not known and the pre-irradiation dark current cannot be subtracted. Consequently, for CIS A, we represent dark current distributions normalized with respect to the ionization peak (pixels which do not contain any bulk defects and which dark current increase is due only to ionization). In that case, the ionization induced dark current (which is believed to be similar in all the pixels of the CIS [20]) is roughly subtracted and the remaining dark current increase corresponds only to displacement damage effects.

TABLE II: IRRADIATION FLUENCES AND ENERGIES

CIS	Fluence determined from ionization spots (α/cm²)	Alpha particle energy in photodiode
A	2.10^8	4 MeV
A	$6.5.10^8$	4 MeV
A	$1.5.10^9$	4 MeV
B	1×10^9	4 MeV
B	4×10^9	4 MeV
B	1×10^{10}	4 MeV
B'	1×10^8	< 500 keV
B'	7×10^8	< 500 keV
B'	2×10^9	< 500 keV

In order to exceed the limitations of the COTS CIS, two identical custom CISs B and B' fabricated in a commercially available 0.18 µm process designed for imaging are also irradiated (Table I). These CISs are 256x256 pixel PPD CIS with very low intrinsic dark current (about 3 e^-/s at 22°C), providing a very good dark current increase resolution. They have fewer pixels than CIS A but allow a full control of the CIS operation conditions (operating voltages, image acquisition and readout timings) and give access to the absolute dark current value. Hence, for CIS B and B', the dark current increase distribution before and after irradiation can be plotted. The dark current is obtained by acquiring sets of 100 images at different integration times, and the dark current is obtained by a linear fit on the first 20% of the pixel Full Well

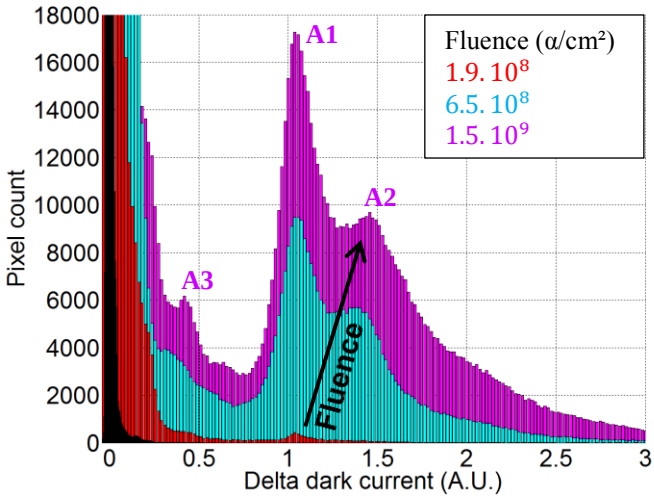

Figure 1: Dark current histogram normalized on the ionization peak for CIS A at different irradiation fluences and at T=22°C.

Capacity (FWC) to avoid saturation and dark current non-linearity [21].

B. Irradiation setup and particle energies tested

The radiation source is a 30 kBq activity ^{241}Am source, emitting alpha particles of 5.5 MeV. Table II presents the particle fluences at different irradiation steps in each CIS. CIS A is irradiated unbiased, with the source placed in air at 6 mm above the CIS. In that case, the particles go through the photodiodes with an energy of 4 MeV (estimated with SRIM [22] accounting for the 6 mm of air and 5 µm of silicon dioxide above the photodiodes). CIS B is irradiated unbiased in the same configuration as CIS A, and CIS B' is irradiated with the source placed 28 mm above the CIS instead of 6 mm. CIS B' is irradiated unbiased, except during the first fluence step in order to observe the formation of the defects by monitoring the dark signal of the pixels (see section III.C).

In that case, the particles stop inside (or very close to) the depleted volume of the photodiodes. Indeed, they lose almost all their energy in the air and silicon dioxide and reach the depleted volume with energy lower than 500 keV. This was verified by measuring the size of the ionization spots on the experimental images during the irradiation, which are generated by the formation of electron-hole pairs in the pixels on the particle trajectory. Most of the ionization spots were confined into single pixels, which mean that most of the particles stopped before the bottom of the depleted volume of the photodiode. The aim of this second configuration is to minimize the ionization induced dark current for a given DDD, because the NIEL to LET ratio increases for decreasing particle energy. Moreover, the dark current distributions of CIS B and B' can be compared to see the bulk defect population depends on the alpha particle energy.

The fluences reported in Table II are calculated from the number of ionization spots detected on the biased image sensor during a short period of time under irradiation. For CIS B' (end-of-range alphas), the particles stop at various depths within the depleted volume (because they do not have exactly the same projected range), hence they deposit different DDD.

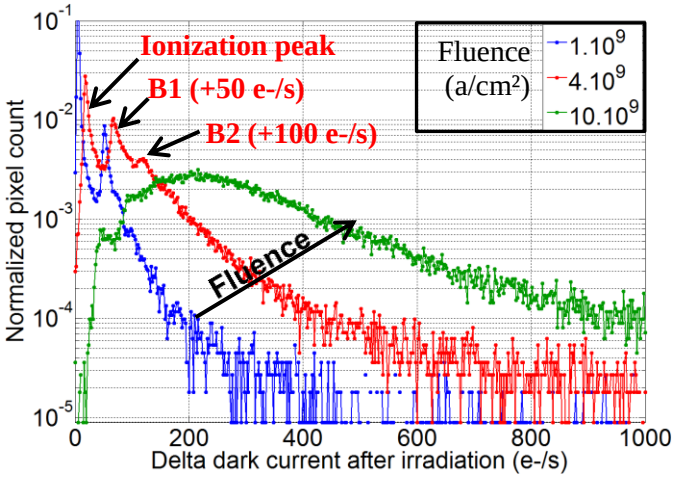

Figure 2: Delta dark current distributions for CIS B at several fluences and at T=22°C. Two DCS peaks can be observed at 50 e-/s and 100 e-/s.

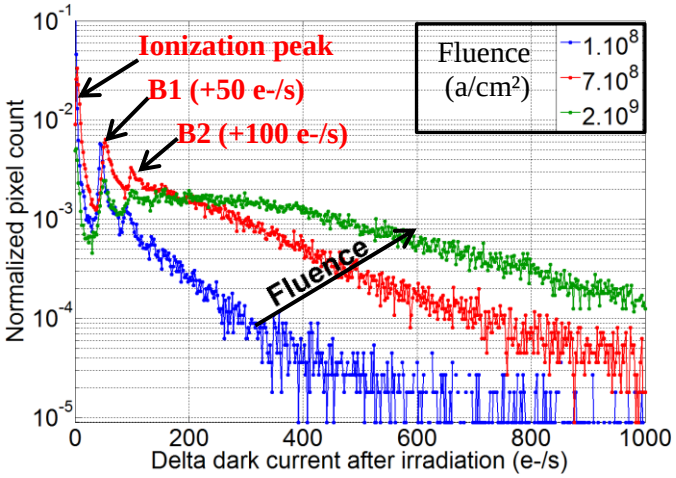

Figure 3: Delta dark current distributions for CIS B' at several fluences and at T=22°C. Two DCS peaks can be observed at 50 e-/s and 100 e-/s.

Therefore, the total DDD cannot be precisely calculated for CIS B'. However, radiation dose is not of primary interest for the main goal of this study: demonstrate that DCS can be used to identify radiation induced defect in irradiated CIS.

III. Experimental Results

A. Irradiation of the COTS CIS (CIS A)

Fig. 1 presents the dark current histogram for CIS A at T=22°C and at different irradiation fluences. At the highest fluence, three dark current peaks are observed and located at dark current values of 1 A.U. (peak A1), 1.4 A.U (peak A2) and 0.4 A.U. (A3). The dark current position of the peaks does not change with fluence but their height increases, which means that they correspond to specific dark current increases from particular defects in the pixels. Since the sum of the dark current of A1 and A3 is close to the dark current of A2, A2 could correspond to pixels which contain both A1 and A3 defects.

B. Irradiation of the custom CIS (CIS B and B')

Fig. 2 presents the dark current increase distributions in logarithmic scale for CIS B at T=22°C and at different

TABLE III: MEAN DARK CURRENT INCREASE

CIS	Fluence determined from ionization peaks (α/cm²)	Mean dark current increase at 22°C (e-/s)
B	1×10^9	35
B	4×10^9	160
B	1×10^{10}	480
B	Annealing at 200°C	80
B	Annealing at 260°C	70
B'	1×10^8	35
B'	7×10^8	200
B'	2×10^9	440
B'	Annealing at 170°C	160
B'	Annealing at 200°C	75
B'	Annealing at 240°C	55
B'	Annealing at 280°C	45

fluences. The first peak on the left (lowest dark current increase) must correspond to pixels which do not contain any radiation-induced bulk defects. This peak quantifies ionization induced dark current, which is believed to be similar in all the pixels of the CIS (ionization usually produces a Gaussian dark current increase distribution [20]). Hence, the generation rate of the single bulk defects represented by the DCS peaks correspond to the delta dark currents with respect to the ionization peak. At 1.10^9 α/cm², only one DCS peak noted B1 is detected 50 e-/s after the ionization peak and should correspond to pixels which contain a particular defect (which we call "B1 defect") generating 50 e-/s. At 4.10^9 α/cm², a second peak noted B2 is visible at 100 e-/s after the ionization peak, which could correspond to pixels which contain exactly two B1 defects.

At 1.10^{10} α/cm², B1 and B2 are almost not visible anymore and the distribution starts to be distorted, towards a Gaussian shape rather than an exponential shape. This transformation suggests that most of the pixels now contain several defects, which is supported by the fact that the mean dark current increase (480 e-/s) is much higher than the generation rate of the main single defect detected by DCS here (50 e-/s for B1).

Fig. 3 presents the dark current distributions for CIS B' irradiated with end-of-range (< 500 keV) alpha particles. The dark current peaks at +50 e-/s (B1) and +100 e-/s (B2) are also detected, suggesting that end-of-range alpha particles produce similar bulk defects than 4 MeV alpha particles. Table III presents the mean dark current increase after various irradiation fluences in CISs B and B' (as well as after various annealing steps, see section III.E.). The mean dark current increase is 5 to 10 times higher in CIS B' than in CIS B for a given fluence, which means that an alpha particle stopping in the depleted volume produces 5 to 10 times more displacement damage than a 4 MeV alpha particle crossing the photodiode. This is in agreement with the fact that the NIEL increases with decreasing particle energy, leading to a large displacement damage deposition at the particle end-of-range. By integrating the NIEL over the last 300 nm of the particle range (which is roughly the PPD depleted depth for our CIS B), we find that about 4 keV of DDD is deposited [20], whereas a 4 MeV alpha deposits only 30 eV along 300 nm.

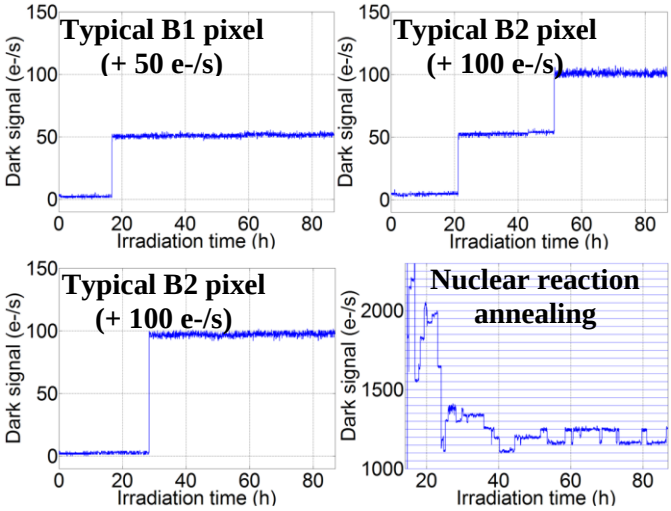

Figure 4: Dark signal of a pixel belonging to B1 (a), two pixels belonging to B2 (b, c), and a hot pixel (d) in CIS B' at T=22°C.

This is more than a factor 100 between the two cases, but the end-of-range alpha particle stopping right at the end of the depleted volume in the best case scenario. Indeed, the longitudinal straggling of 5.5 MeV alphas travelling through 28 mm of air and 5 µm of silicon dioxide is about 1 µm. Hence, many end-of-range alpha particles will stop at the beginning of the depleted volume, or after the end of the volume, and will deposit much less displacement damage than the worst case scenario.

In both CIS, the right part of the dark current distribution (hot pixel tail) has an exponential shape, which is also usually observed in CIS irradiated with high-energy protons [2], high-energy neutrons [2, 23] and low-energy neutrons [23]. This exponential hot pixel tail does not contain any DCS peaks; hence it seems to correspond either to the superimposition of many defects in the pixels or to other defects which can have many different generation rates.

C. Dark signal during irradiation in CIS B'

The first fluence step in CIS B' (up to 1.10^8 α/cm²) lasted 88 hours and was performed biased in order to measure the dark signal of the pixels during irradiation (Fig. 4). This technique was previously used to investigate the short term annealing of dark current increases produced in neutron [24] and alpha [25] irradiations. Here, it allows observing the formation of the defects which generate dark current. Fig. 4 presents the dark signal of four different pixels of CIS B' during irradiation. Each data point is the average of one hundred successive images of one second integration time each, in order to smooth the dark current temporal noise and to remove ionization effects (ionization spots when particles cross the pixel). The dark signal of a pixel which belongs to the DCS peak B1 after irradiation (50 e-/s after the ionization peak) is shown in Fig. 4.a. A dark signal step of +50 e-/s is observed at a given time, which corresponds to the formation of a single defect. This shows that the dark current in B1 pixels is due to a single defect and not to a cumulative effect. Fig. 4.b and 4.c present the dark signal of two pixels which

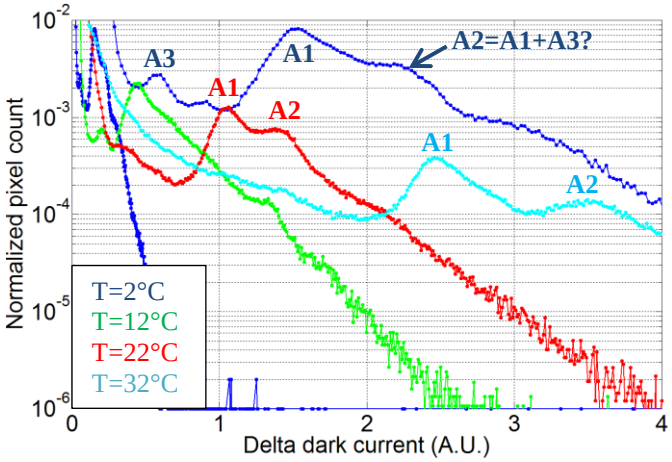

Figure 5: Dark current distributions for CIS A at a fluence of $6.5.10^8$ a/cm². The distribution at 2°C is represented at its original position and also with a 10:1 dark current scale to magnify the peaks.

belong to the DCS peak B2. Either two separated dark current steps of +50 e-/s are observed (fig. 4.b) or a unique dark current step of +100 e-/s (fig. 4.c). The first case corresponds to the formation of two B1 defects at different times and proves that at least a part of B2 corresponds to pixels which contain two B1 defects. The second case suggests that either two B1 defects form during the same image (and thus that one alpha particle can create several B1 defects simultaneously), or that another defect with a generation rate of 100 e-/s exists. We should note that there is about the same number of pixels belonging to each case (4.b or 4.c) among the B2 pixels.

Eventually, fig 4.d shows the typical dark signal of a very hot pixel, which has most likely encountered a nuclear scattering event (which is rare for 4 MeV alphas but not impossible). The dark current increase is several thousand of e^-/s, like usually observed for nuclear scattering events produced by neutrons or high energy protons [2, 23-24]. The dark signal after the nuclear event shows many 50 and 100 e^-/s steps (horizontal blue lines in fig. 4.d are separated by 50 e^-/s), which suggests that many defects similar to defects B1 and B2 were created by the nuclear interaction. Some of these defects seem unstable or seem to show Random Telegraph Signal (RTS) behavior [20].

D. Activation energy of the dark current peaks

In order to identify the defects responsible for the DCS peaks, we need to determine their energy level in the bandgap. The variation of the generation rate U of a defect with temperature can be simply expressed as:

$$U \; \alpha \; \exp(-\frac{qE_a}{kT}) \quad (1)$$

E_a is the activation energy of the generation rate. E_a depends on the energy level of the defect but also on the variation of ${n_i}^2$ and E_g with temperature, and from the SRH formalism [3] a simplified equation can be extracted:

$$|E_t - E_i| \simeq E_A - 0.63 \; eV \quad (2)$$

E_t is the energy level of the defect and E_i is the middle of the bandgap. If a pixel contains only one type of defect (and if the ionization induced dark current is negligible compared to the generation rate of the defects), then the activation energy of

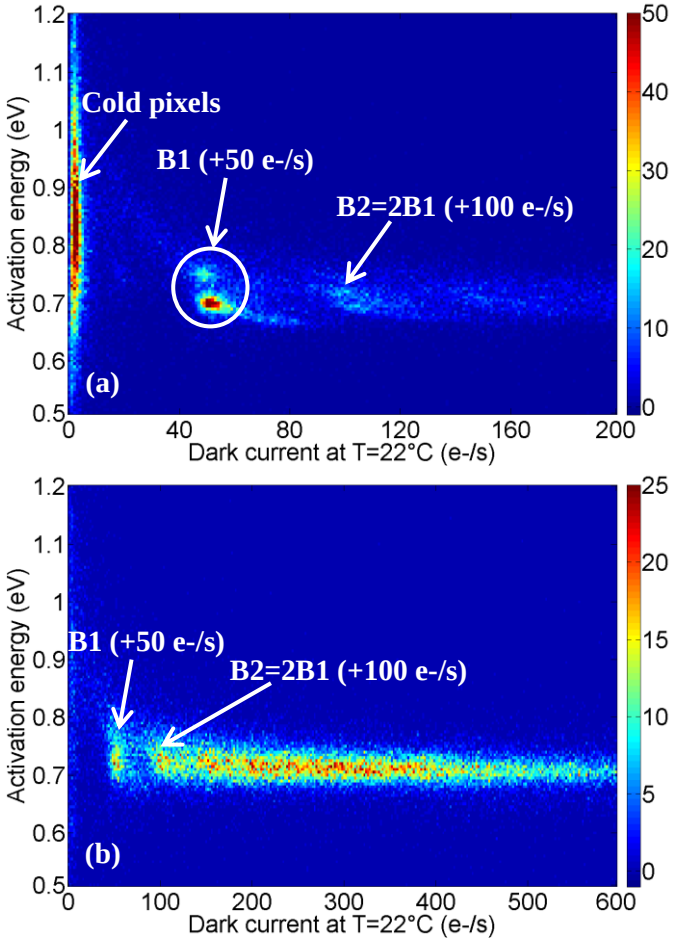

Figure 6: Scatter of the dark current increase activation energy as a function of dark current increase at T=22°C for CIS B' at a fluence of a) 2.10^8 a/cm² and b) 2.10^9 a/cm².

the dark current is equal to the activation energy of the generation rate of the defects, and E_t can be deduced.

Fig. 5 presents the dark current distribution of CIS A irradiated at $6.5.10^8$ α/cm² at different temperatures between 2°C and 32°C. The activation energy of the dark current is calculated from Eq. 1 by plotting the variation of the dark current as a function of temperature in logarithmic scale (Arrhenius plot not shown here) and extracting the slope. The dark current of peaks A1 and A2 have activation energies of respectively 0.67 and 0.66 eV (A3 is too dim to extract the activation energy), which suggests that the responsible defects have energy levels very close to the middle of the bandgap.

In fig. 6, the scatter of the dark current increase activation energy (determined on the temperature range from -8°C to 22°C) of all the pixels of CIS B' is represented as a function of dark current at T=22°C at two different fluences. At 2.10^8 a/cm², the pixel cluster on the left corresponds to pixels without bulk defects (ionization peak). There are two clusters of pixels located at +50 e-/s (a large one at 0.70 eV and a small one at 0.75 eV), which both correspond to peak B1 but have different activation energies. Thus, it seems that B1 comprises pixels which can contain two different defects with similar generation rates. B2 is also visible at 100 e-/s and at similar activation energy than B1, suggesting that it corresponds to pixels which contain two B1 defects as

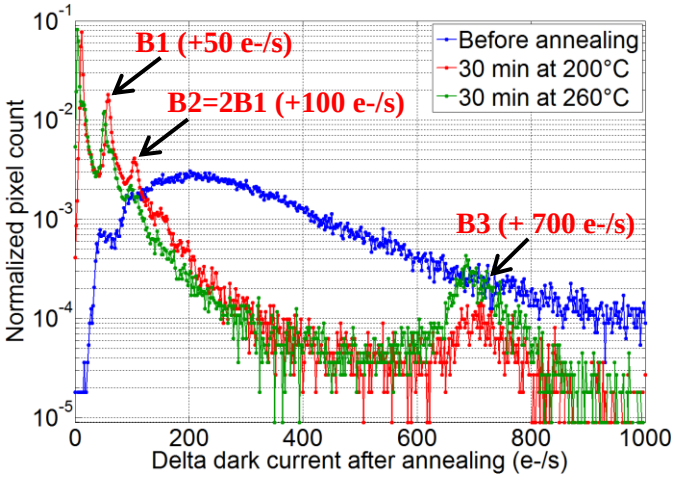

Figure 7: Delta dark current distributions at T=22°C for CIS B before and after isochronal annealing at 200°C and 260°C.

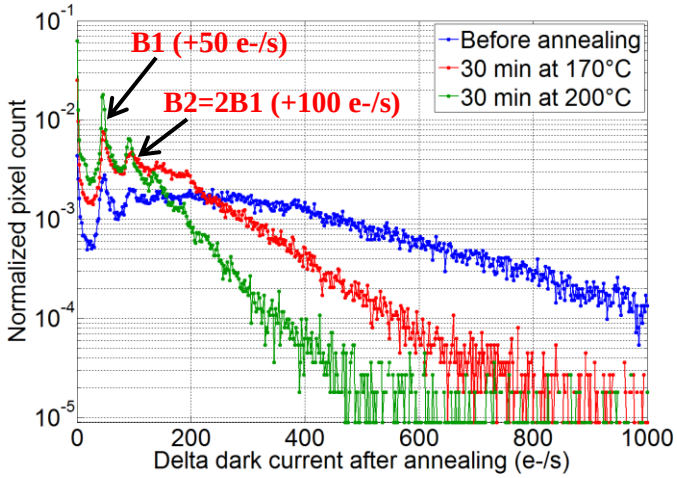

Figure 8: Delta dark current distributions at T=22°C for CIS B' before and after isochronal annealing.

assumed before. At 2.10^9 a/cm², the ionization peak cluster has disappeared because all the pixels contain bulk defects. The dark current activation energy is about 0.70 eV for all the pixels (and also for hot pixels), which suggest that the dark current of all the pixels is the superimposition of many B1 defects.

E. Isochronal annealing of CISs B and B'

We studied the stability of the defects with temperature by performing an isochronal annealing (from 100°C to 280°C by 30-minute steps every 20 or 30°C) on the irradiated CIS. The annealing temperature of the defects can be determined and compared to literature in order to identify them. Fig. 7 presents the dark current distributions of CIS B before annealing (after the highest fluence of 1×10^{10} a/cm²) and after 200°C and 260°C annealing steps. First of all, a very good annealing of the TID induced dark current is observed because the ionization peak shifts from 50 e-/s before annealing down to 11 e-/s after 200°C annealing and 4 e-/s after 260°C annealing. The displacement damage dark current increase has also annealed a lot and is divided by six after 200°C annealing (see Table III). In the previous section, it was suggested that hot pixels could contain many B1 defects because they have the same dark current activation energy than the B1cluster (see fig. 6.b). In fig. 7, we can see that the hot pixel tail has annealed a lot after 200°C annealing, which suggests that the main B1 defect (main pixel cluster at 0.70 eV in fig. 6.b) is not stable at 200°C. On the other hand, since peaks B1 and B2 are still visible after 200°C in fig. 7, the second B1 defect (small pixel cluster at 0.75 eV in fig. 6.a) is stable. The height of B1 and B2 has increased after annealing in fig. 7 because many hot pixels have annealed and now contain only one or two remaining B1 defects. Some of them have also completely annealed, which is why the ionization peak appears again after annealing.

B1 and B2 have decreased after 260°C annealing, which means that the B1 defect which was still stable after 200°C (0.75 eV cluster in fig. 6.a) annealing starts to anneal at 260°C. Once again, B2 seems to correspond to two B1 defects because the peaks B1 and B2 start to decrease at the same annealing step. Eventually, another DCS peak B3 appears at 700 e-/s after 200°C annealing, and the defect seems stable at least up to 260°C.

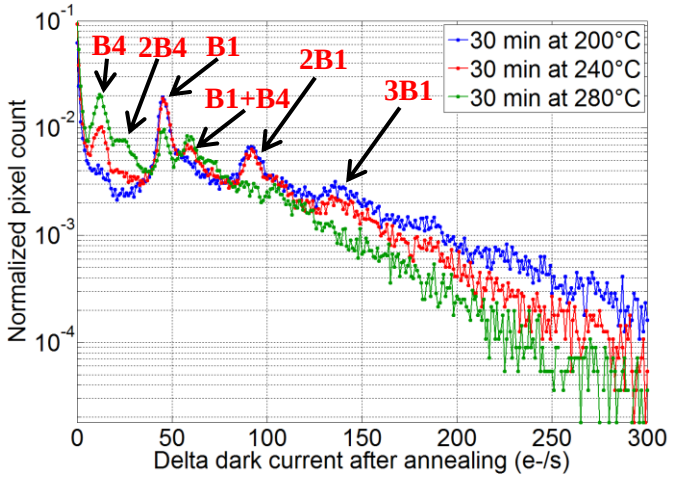

Figure 9: Delta dark current distributions at T=22°C for CIS B' after isochronal annealing at higher temperatures than in Fig.8.

Fig. 8 shows the dark current distributions of CIS B' before and after isochronal annealing at 170°C and 200°C. A similar behavior than in CIS B is observed, with a strong hot pixel tail annealing and increasing DCS peaks B1 and B2. Fig. 9 shows the dark current distributions after higher temperature annealing. B1 and B2 have the same height after 200°C and 240°C, which means that the B1 defect which has not annealed below 200°C (0.75 eV cluster in fig. 6.a) is stable up to 240°C. B1 and B2 start to decrease after 260°C annealing, hence this defect starts to dissolve at 260°C as observed in CIS B. After 240°C annealing, a new DCS peak B4 appears at +13 e-/s, and corresponds to another defect. A DCS peak is also visible at +13 e-/s after B1, which corresponds to pixels containing both B1 and B4 defects. After 280°C, the peak B4 has increased another peak is visible at +26 e-/s (pixels with two B4 defects). Eventually, another peak is visible at 26 e-/s after B4, which corresponds to pixels containing one B1 defect and two B4 defects. The idea that B4 starts to appear when B1 starts to disappear suggests that B4 is formed from B1. It is possible that B1 liberates specific impurities when dissolving (which are used to form B4), or that B1 transforms

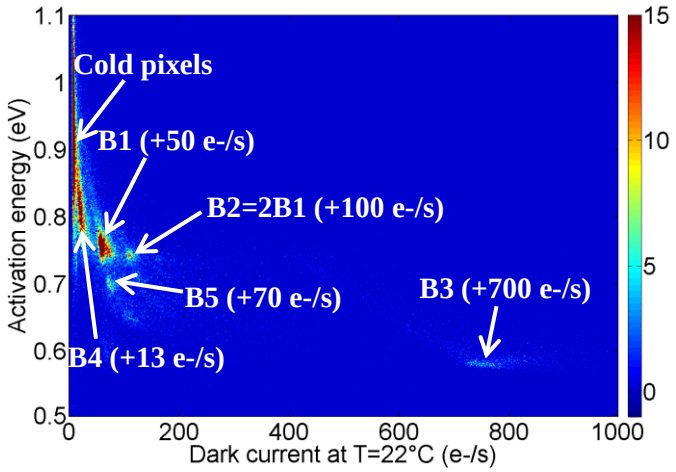

Figure 10: Scatter of the dark current increase activation energy against dark current at T=22°C after 260°C annealing for CIS B.

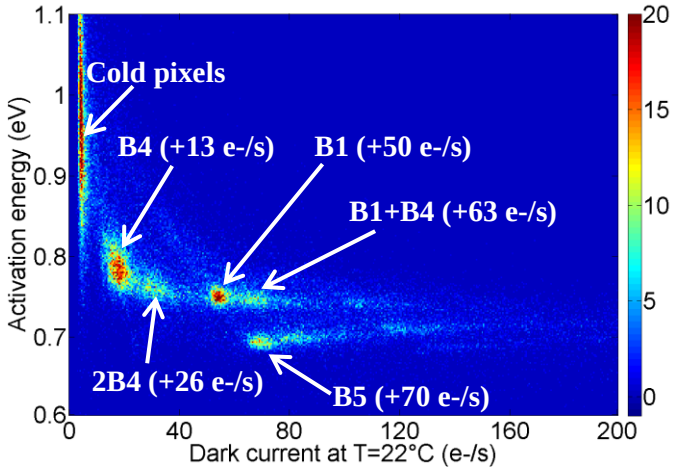

Figure 11: Scatter of the dark current increase activation energy against dark current at T=22°C after 280°C annealing for CIS B'.

into B4 by absorbing elements which are now mobile (or by diffusing to them).

We have also annealed a non-irradiated CIS at 280°C during 30 minutes to see if the same bulk defects appeared. Before annealing, the non-irradiated CIS dark current distribution does not contain hot pixels or DCS peaks and is a simple Gaussian distribution centered on 3 e-/s at 22°C. It is unchanged after 280°C annealing, which suggests that all the bulk defects detected by DCS after irradiation and during isochronal annealing require prior radiation damage.

F. Activation energy after isochronal annealing

The activation energy of the dark current can be measured again after annealing to determine the energy level of the new defects and to detect which defects have disappeared during annealing. Fig. 10 represents the activation energy of the dark current after 260°C annealing in sensor B. The new defect B3 is visible at +750 e-/s and has dark current activation energy of 0.60 eV. Fig. 11 presents the activation energy of the dark current increase after 280°C annealing in sensor B'. The main pixel cluster observed at +50 e-/s and 0.70 eV in fig. 6 has completely disappeared and only the cluster at 0.75 eV remains. The same transformation is observed in sensor B (fig. 10). Hence, the major B1 defect with the activation energy of

TABLE IV: DEFECTS DETECTED BY DCS

Defect	Generation rate at T=22°C (e-/s)	Generation rate activation energy	Energy level from Ec
B1	50	0.70 eV	0.49 eV
B1	50	0.75 eV	0.44 eV
B3	700	0.60 eV	0.56 eV
B4	13	0.80 eV	0.39 eV
B5	70	0.70 eV	0.49 eV

TABLE V: RADIATION-INDUCED BULK DEFECTS IN SILICON WITH CLOSE-TO-MIDGAP ENERGY LEVELS

Defect	Energy level	Formation
VP	Ec – 0.46 eV [29]	V + P (after irrad.) [12]
V_2(-/0)	Ec – 0.42 eV [29]	V + V (after irrad.) [12]
V_2O	Ec – 0.55 eV [34]	V_2 + O (220°C) [32]
V_2O(-/0)	Ec – 0.42 eV [32]	V_2 + O (220°C) [32]
V_2O_2	Ec – 0.43 eV [32]	$V_2O \rightarrow VO + V$ (300°C) $2VO \rightarrow V_2O_2$ [32]
V_2H	Ec – 0.43 eV [31]	V_2 + H [31]
V_2H	Ec – 0.45 eV [31]	V_2 + H [31]

0.70 eV (large cluster in fig. 6) anneals below 260°C (as suggested in the previous section) whereas the defect with the activation energy of 0.75 eV is still stable. Eventually, the new defects B4 is observed in both CIS at +13 e-/s and about 0.80 eV and another defect B5 is visible at +70 e-/s and 0.70 eV. Table IV summarizes the generation rates and activation energies of the bulk defects detected in this study.

IV. DISCUSSION

A. Comparison of the DCS peaks in CIS A and B

It was observed that the main DCS peak of CIS A (A1) has a dark current of 1 A.U. at T=22°C. If the analog gain in the dark was equal to 2 as suggested in section II.A, 1 A.U. should correspond to 50 e-/s for CIS A. and peak A1 of CIS A would correspond to peak B1 of CISs B and B'. The activation energies of peaks A1 and B1 are quite close (respectively 0.67 and 0.70 eV) and are likely to correspond to the same defect. Moreover, the peaks A2 and A3 of CIS A could correspond respectively to the peaks B5 and B4 observed in CIS B' after isochronal annealing.

B. Identification of the defects in CIS B and B'

The radiation-induced bulk defects in silicon which have an energy level close to the middle of the bandgap (i.e. which supposedly have a significant generation rate) are summarized in Table V from literature [12, 17-19, 27-34].

We have seen in section III.D that the main DCS peak B1 detected in CIS B and B' actually corresponds to two different defects. By comparing Table IV and V, we can see that these two defects could be the divacancy V_2 and the vacancy-phosphorus complex VP, because they exist after irradiation [12] and because the energy levels correspond well to our results. Moreover, according to literature, V_2 is likely to have a dark current generation rate of 50 e-/s at T=22°C. For example, in [17], a defect with a generation rate of 42 e-/s was detected in 1-MeV proton irradiated silicon and attributed to V_2. A DCS peak at 40 e-/s was also detected and attributed to

V_2 in a 120-MeV proton irradiated CIS [2]. In [12], a defect detected by DCS in alpha irradiated CCD in identified as V_2 has an energy level of $E_c - 0.44$ eV and a generation rate of 1200 e-/s at T=60°C. This energy level corresponds to the 0.75 cluster observed for B1 in fig. 6, and the generation rate at T=22°C can be estimated using eq. 1 with E_a = 0.75 eV; we find U = 42 e-/s, which is close to [2, 17] and to our measurement of 50 e-/s for B1. Thus, it seems that the B1 pixel cluster at 50 e-/s and 0.75 eV in fig. 6 is the divacancy.

In [12], the dark current distribution before annealing in alpha irradiated CCD displays two main DCS peaks at respectively 1,000 e-/s and 1,200 e-/s, attributed to respectively VP and V_2. The energy level of VP is measured at $E_c - 0.46$ eV in [12], which is similar to the energy level of the defect responsible for the B1 cluster at 0.70 eV in fig. 6 ($E_c - 0.49$ eV). The generation rate activation energy of VP is 0.73 eV in [12] (from eq. 2) and its generation rate at T=22°C should be 38 e-/s using (from eq. 1). This is very close to the calculated generation rate of V_2 at 22°C (42 e-/s), which shows that these two defects are likely to have a similar generation rate at 22°C. Thus, it is likely that the pixel cluster at 50 e-/s and 0.70 eV in fig. 6 corresponds to VP. According to literature, the energy level of VP is 0.03 to 0.05 eV higher than energy level of V_2, which is in agreement with the generation rate activation energy difference observed in fig. 6 (respectively 0.70 and 0.75 eV for VP and V_2). In [12], the concentration of V_2 and VP was roughly equal after irradiation. Because we use PPD CIS, the phosphorous doping level is likely to be higher than in the CCD used in [12], which could explain why the 0.70 eV cluster in fig. 6 (VP) is more populated than the 0.75 eV cluster (V_2) after irradiation.

We can also calculate the emission cross section of the defects to compare to literature. Indeed, the generation rate can be simply expressed from the emission cross section and energy level as [3]:

$$U \sim \frac{\sigma v_{th} n_i}{2\cosh\left(\frac{|E_t - E_i|}{kT}\right)} \quad (3)$$

The electron thermal velocity and intrinsic carrier concentration are $v_{th} \sim 2.3.10^5\ m/s$ and $n_i \sim 10^{10} cm^{-3}$ at 300K. We find $\sigma \sim 3.10^{-15} cm^2$ for VP (50 e-/s and $E_t - E_i$ = 0.07 eV) and $\sigma \sim 2.10^{-14} cm^2$ for V_2 (50 e-/s and $E_t - E_i$ = 0.12 eV). These emission cross sections have values similar to what can be found in literature for V_2 and VP [12, 29 and 30].

Defect B3, which appears after 200°C annealing, has a generation rate activation energy of 0.60 eV (fig. 10) which is below the lowest possible activation energy (0.63 eV for a midgap defect from eq. 2). This suggests that the generation rate of defect B3 is enhanced somehow, possibly by inter-center charge transfer [26], which could explain why its dark current generation rate is very high for a single defect. Otherwise, B3 must still have an energy level very close to midgap and could correspond to the divacancy-oxygen complex (V_2O), which has an energy level at $E_c - 0.55$ eV as reported in Table V [34]. Defect B3 is detected in CIS B (4 MeV alpha particles going through the photodiode down to the substrate) but not in CIS B' (end-of-range alpha particles stopping in the photodiode). A possible explanation is that the oxygen concentration is much higher in the substrate than in the epitaxy which is more pure. Hence, many V_2O defects can be formed with 4 MeV alpha particles in the substrate, and then diffuse to the depleted volume during isochronal annealing.

The annealing behavior can help identify the defects. First of all, B1 started to anneal at 260°C which is close to the annealing temperature of V_2 according to literature [29-30]. This is also what is observed in [12] for the defect identified as V_2, which starts to anneal at 270°C. On the other hand, the defect identified as VP in [12] anneals at 150°C (which agrees with literature). This explains why the B1 cluster at 0.70 eV observed before annealing (identified as VP) has completely disappeared after 260°C annealing. This also explains why the mean dark current increase has already greatly reduced after 200°C annealing (all the VP defects have already annealed after 200°C annealing).

In [12], the annealing of V_2 at 270°C is accompanied by the formation of new defects at a position similar to defect B4 in the dark current distribution. In [12], these defects are attributed to V_2O or V_2H complexes with energy levels of respectively $E_c - 0.43$ eV and $E_c - 0.44$ eV. These two defects were also found elsewhere in the literature with similar energy levels (Table V). Thus, defect B4 could correspond to one of these defects, or to other defects such as V_2O_2 which also has a similar energy level (Table V). Eventually, defect B5 may also correspond to one of the defects reported in Table V such as V_2O, V_2H or V_2O_2.

The fact that B4 and B5 start to appear when V_2 starts to anneal suggests that B4 and B5 form from V_2. It is possible that impurities such as O, H or O2 become mobile at 260°C, diffuse in the bulk, and combine with V_2 to replace it by V_2O, V_2H or V_2O_2. Inversely, it is also possible that V_2 becomes mobile and diffuses until being captured by an impurity to form a new defect [31]. This last idea is supported in several work [31-34] which suggest that V_2 becomes mobile around 200°C and associates with interstitial oxygen atoms to form V_2O or with hydrogen atoms to form V_2H [31]. This suggests again that B3 (which appears after 200°C annealing) could correspond to V_2O with an energy level very close to midgap ($E_c - 0.55$ eV), justifying its high generation rate of 700 e-/s. Then, at 260°C, the annealing temperature of V_2 is reached [12] and it is likely that V_2 starts to dissociate, releasing vacancies which can form other defects such as VO, VH or VOH by combining with impurities. However, these defects do not have energy levels close to the middle of the bandgap and cannot correspond to B4 and B5. Another possibility is that V_2O starts being mobile, associating with another oxygen atom to form V_2O_2. V_2O could also dissociate into VO and V, leading to associations of two VO to form V_2O_2 or to associations of VO and H to form VOH [31]. However, this would suggest that B3 does not correspond to V_2O because B4 and B5 are observed in both CIS even if B3 is not observed (CIS B). In conclusion, the identities of B3, B4 and B5 remain unknown but it is likely that B3 corresponds to V_2O and that B4 and B5 form from V_2 or V_2O.

C. Probability of formation of the defects

In CIS B irradiated at a fluence of 1×10^9 a/cm² (fig. 2), the peak B1 (which corresponds to pixels which contain either V_2 or VP) contains about 7% of the total number of pixels. Because the defects are distributed randomly in the pixels,

some pixels contain two B1 defects (the defect distribution follows a Poisson distribution). Hence, the total number of V_2 and VP defects is .08 times the number of pixels. The depleted volume of the photodiode is about 0.8 μm^3 for CIS B (determined from other irradiation results on this CIS [23]). According to SRIM [22], an average of 2 vacancies (Frenkel pairs) is created over a one micron travel for a 4-MeV helium ion. By multiplying the fluence, the depleted volume and the number of vacancies per unit length, we find that about 15 vacancies are created in each photodiode of CIS B irradiated at 1×10^9 a/cm². Hence, the defect to vacancy ratio is 1/190 (0.5%). According to [16], more than 90% of the Frenkel pairs recombine right after irradiation and not all the surviving ones lead to the formation of SRH R-G centers. Indeed, it was previously observed that the ratio between V_2 and radiation-induced Frenkel pairs is about 1% for alpha particles in silicon [18]. In [12], this ratio is 0.2% by comparing the number of V_2 and VP to the total number of vacancies introduced (estimated with SRIM [22]). Our result of 0.5% is similar to these other results, suggesting again that B1 corresponds to V_2 and VP.

In CIS B after 1×10^9 a/cm² irradiation, the mean dark current increase due to displacement damage is about 30 e-/s (Table III) but the mean dark current generated by the major bulk defects (V_2 and VP) is only 4 e-/s (because the total number of V_2 and VP is about 0.08 times the number of pixels and they both generate 50 e-/s). Hence, the major bulk defects detected by DCS seem to account for only 10 to 15% of the total mean dark current increase due to displacement damage. Consequently, there seem to be many other defects which are not detected by DCS (especially in the hot pixel tail after the DCS peaks, at higher generation rates) which greatly contribute to the dark current increase.

V. Conclusion

Dark Current Spectroscopy (DCS) was tested for the first time on irradiated CIS to study radiation-induced bulk defects in silicon. It was tested on two different PPD CIS (a COTS CIS from OmniVision and two identical custom CIS) and at two different alpha particle energies in the custom CIS (4 MeV and < 500 keV). Several DCS peaks were observed in the dark current distributions of both CIS. In the custom CIS, the formation of the bulk defects could be detected by measuring the evolution of the dark signal of the pixels during irradiation. Two major radiation-induced bulk defects were detected by DCS after irradiation and were similar for 4 MeV and end-of-range alpha particles. By measuring the activation energy of the dark current of the pixels containing these defects, we could determine their energy levels and they could be identified as the divacancy (V_2) and the vacancy-phosphorus complex (VP). Their identity was also verified by performing an isochronal annealing, which showed that VP and V_2 annealed at temperatures consistent with literature. Another defect appeared after 200°C annealing but only for 4 MeV alphas, which suggests that it uses oxygen which is present mainly in the substrate; it could correspond to V_2O because of its high generation rate. Eventually, for both alpha particle energies, two other bulk defects started to appear around 260°C. It is likely that they form from V_2 and/or V_2O which could start to diffuse and/or to anneal. These new defects could be complexes such as V_2O, V_2H or V_2O_2, which have energy levels close to the middle of the bangdap.

References

[1] V. Goiffon, C. Virmontois, P. Magnan, P. Cervantes, S. Place, M. Gaillardin, S. Girard, P. Paillet, M. Estribeau and P. Martin-Gonthier, "Identification of Radiation Induced Dark Current Sources in Pinned Photodiode CMOS Image Sensors," *IEEE Trans. Nucl. Sci.*, vol. 59, no. 4, pp. 918-926, 2012.

[2] C. Virmontois, V. Goiffon, P. Magnan, S. Girard, O. Saint-Pe, S. Petit, G. Rolland and A. Bardoux, "Similarities between Proton and Neutron Induced Dark Current Distribution in CMOS Image Sensors," *IEEE Trans. Nucl. Sci*, vol. 59, no. 4, pp. 927-936, Aug. 2012.

[3] C.-T. Sah, R. N. Noyce and W. Shockley, "Carrier generation and recombination in pn junctions and pn junction characteristics," *Proc. of the IRE*, vol. 45, no. 9, pp. 1228–1243, 1957.

[4] R. D. McGrath, J. Doty, G. Lupino, G. Ricker and J. Vallerga "Counting of deep-level traps using a charge-coupled device," *IEEE Trans. Nucl. Sci.*, vol. 34, no. 12, pp. 2555–2557, 1987.

[5] H. I. Kwon, I. M. Kang, B.-G. Park, J. D. Lee and S. S. Park, "The Analysis of Dark Signals in the CMOS APS Imagers from the Characterization of Test Structures," *IEEE Trans. Elec. Dev.*, vol. 51, no. 2, pp. 178-184, Feb. 2004.

[6] W. C. McColgin, J. P. Lavine, J. Kyan, D. N. Nichols and C. V. Stancampiano, "Dark current quantization in CCD image sensors," *International Electron Devices Meeting*, pp. 113-116, 1992.

[7] W. J. Toren, J. Bisschop, "Metal contamination characterization in CCD image sensors," *International Electron Devices Meeting*, pp. 163–166, 1995.

[8] E. A. G. Webster, R. L. Nicol, L. Grant and D. Renshaw, "Per-Pixel Dark Current Spectroscopy Measurement and Analysis in CMOS Image Sensors," *IEEE Trans. Elec. Dev.*, vol. 57, no. 9, pp. 2176-2182, Sep. 2010.

[9] F. Domengie, J.-L. Regolini, P. Morin and D. Bauza, "Impact on device performance and monitoring of a low dose of tungsten contamination by dark current spectroscopy," in *IEEE International Reliability Physics Symposium (IRPS)*, pp. 259–264, 2010.

[10] J.-P. Carrere, S. Place, J.-P. Oddou, D. Benoit and F. Roy, "CMOS image CIS: Process impact on dark current," *IEEE International Reliability Physics Symposium (IRPS)*, pp. 3C.1.1 - 3C.1.6, 2014.

[11] F. Domengie, P. Morin and D. Bauza, "Modeling the dark current histogram induced by gold contamination in complementary-metal-oxide-semiconductor image sensors," J. Appl. Phys. vol. 118, pp. 024501, 2015.

[12] C. Tivarus and W. C. McColgin, "Dark Current Spectroscopy of Irradiated CCD Image sensors," *IEEE Trans. Nucl. Sci*, vol. 55, no. 3, pp. 1719-1724, Jun. 2008.

[13] I. Jun, M. A. Xapsos and E. A. Burke, "Alpha particle nonionizing energy loss (NIEL)," *IEEE Trans. Nucl. Sci*, vol. 51, no. 6, pp. 3207-3210, Dec. 2004.

[14] C. Poivey and G. Hopkinson, "Displacement Damage Mechanism and Effects", *ESA-EPFL Space Center Workshop*, vol. 9, Jun. 2009.

[15] S. R. Messenger, E. A. Burke, M. A. Xapsos, G. P. Summers, R. J. Walters, Insoo Jun and T. Jordan, "Niel for heavy ions: an analytical approach," *IEEE Trans. Nucl. Sci*, vol. 50, no. 6, pp. 1919-1923, Dec. 2003.

[16] G. P. Summers, E. A. Burke, C. J. Dale, E. A. Wolicki, P. W. Marshall, and M. A. Gehlhausen, "Correlation of particle-induced displacement damage in silicon," *IEEE Trans. Nucl. Sci*, vol. 34, no. 6, pp. 1133–1139, 1987.

[17] P. Hazdra, K. Brand and J. Vobeckỳ, "Defect distribution in MeV proton irradiated silicon measured by high-voltage current transient spectroscopy," *Nucl. Inst. and Methods in Phys. B*, vol. 192, no. 3, pp. 291–300, 2002.

[18] P. Hazdra, J. Rubeš, and J. Vobeckỳ, "Divacancy profiles in MeV helium irradiated silicon from reverse I–V measurement," *Nucl. Inst. and Methods in Phys. B*, vol. *159*, no. 4, pp. 207-217, 1999.

[19] J. Vobecký, P. Hazdra and V. Záhlava, "Impact of the electron, proton and helium irradiation on the forward I–V characteristics of high-power P–i–N diode," *Microelectronics Reliability*, vol. 43, no. 4, pp. 537-544, Apr. 2003.

[20] V. Goiffon, C. Virmontois, P. Magnan, P. Cervantes, F. Corbière, M. Estribeau and P. Pinel, "Radiation damages in CMOS image sensors:

testing and hardening challenges brought by deep sub-micrometer CIS processes," *Proc. SPIE* 7826, CISs, Systems, and Next-Generation Satellites XIV, 78261S, Dec. 2010.
[21] V. Goiffon, M. Estribeau, P. Cervantes, R. Molina, M. Gaillardin and P. Magnan, "Influence of Transfer Gate Design and Bias on the Radiation Hardness of Pinned Photodiode CMOS Image Sensors," *IEEE Trans. Nucl. Sci.*, vol. 61, no. 6, pp. 3290-3301, Dec. 2014.
[22] J. F. Ziegler, M. D. Ziegler and J. P. Biersack, "SRIM – The stopping and range of ions in matter (2010)," *Nucl. Inst. and Methods in Phys. B*, vol. 268, no. 11-12, pp. 1818-1823, Jun. 2010.
[23] J.-M. Belloir, V. Goiffon, C. Virmontois, P. Paillet, M. Raine, O. Duhamel, M. Gaillardin, P. Magnan and O. Gilard, "Pixel Pitch and Particle Energy Influence on the Dark Current Distributions of Neutron Irradiated CMOS Image Sensors," Optics Express, accepted for publication.
[24] M. Raine, V. Goiffon, P. Paillet, O. Duhamel, S. Girard, M. Gaillardin, C. Virmontois, J.-M. Belloir, N. Richard and P. Magnan, "Exploring the Kinetics of Formation and Annealing of Single Particle Displacement Damage in Microvolumes of Silicon," *IEEE Trans. Nucl. Sci.*, vol. 61, no. 6, pp. 2826-2833, Dec. 2014.
[25] E. C. Auden, R. A. Weller, M. H. Mendenhall, R. A. Reed, R. D. Schrimpf, N. C. Hooten and M. P. King, "Single Particle Displacement Damage in Silicon," *IEEE Trans. Nucl. Sci.*, vol. 59, no. 6, pp. 3054-3061, déc. 2012.
[26] S. J. Watts, J. Matheson, I. H. Hopkins-Bond, A. Holmes-Siedle, A. Mohammadzadeh and R. Pace, "A new model for generation-recombination in silicon depletion regions after neutron irradiation," *Nuclear Science, IEEE Trans. Nucl. Sci.*, vol. 43, no. 6, pp. 2587–2594, 1996.
[27] R. Siemieniec, W. Südkamp and J. Lutz, "Determination of parameters of radiation induced traps in silicon," *Solid-State Electronics*, vol. 46, no. 6, pp. 891–901, 2002.
[28] B. G. Svensson, C. Jagadish, A. Hallen and J. Lalita, "Point defects in MeV ion-implanted silicon studied by deep level transient spectroscopy," *Nucl. Inst. and Methods in Phys. B*, vol. *106*, no. 1, pp. 183-190, 1995.
[29] M. Moll, PhD Thesis, "Radiation Damage in Silicon Particle Detectors: Microscopic defects and macroscopic properties," Hamburg University, 1999.
[30] J. Bourgoin, *Point defects in Semiconductors II: Experimental aspects* (Vol. 35), Springer Science & Business Media, 2012.
[31] V. P. Markevich, A. R. Peaker, S. B. Lastovskii, L. I. Murin, and J. L. Lindström, "Defect reactions associated with divacancy elimination in silicon," *Journal of Physics: Condensed Matter*, vol. 15, no. 39, p. S2779, 2003.
[32] J. Coutinho, R. Jones, S. Öberg and P. R. Briddon, "The formation, dissociation and electrical activity of divacancy-oxygen complexes in Si," *Physica B: Condensed Matter*, vol. 340-342, pp. 523-527, Dec. 2003.
[33] M. Mikelsen, E. V. Monakhov, G. Alfieri, B. S. Avset, et B. G. Svensson, "Kinetics of divacancy annealing and divacancy-oxygen formation in oxygen-enriched high-purity silicon," *Physical Review B*, vol. 72, no. 19, Nov. 2005.
[34] I. Pintilie, E. Fretwurst, G. Lindström and J. Stahl "Close to midgap trapping level in 60Co gamma irradiated silicon detectors," *Applied physics letters*, vol. 81, no. 1, pp. 165-167, 2002.